Monthly Notices
of the
ROYAL ASTRONOMICAL SOCIETY

Mon. Not. R. Astron. Soc. **420,** 3017–3025 (2012) doi:10.1111/j.1365-2966.2011.20175.x

An eclipsing post-common-envelope binary in the field of the *Kepler* mission

J. M. Almenara,[1,2,3⋆] R. Alonso,[4] M. Rabus,[1,2,5] C. Lázaro,[1,2] M. J. Arévalo,[1,2] J. A. Belmonte,[1,2] H. J. Deeg,[1,2] T. M. Brown[6] and H. Vázquez Ramió[1,2]

[1]*Instituto de Astrofísica de Canarias, C/ Vía Láctea S/N, E-38200 La Laguna, Spain*
[2]*Departamento de Astrofísica, Universidad de La Laguna, E-38205 La Laguna, Spain*
[3]*Laboratoire d'Astrophysique de Marseille, UMR 6110 CNRS, Technopole de Marseille-Étoile, F-13388 Marseille cedex 13, France*
[4]*Observatoire de Genève, Université de Genève, 51 Ch. des Maillettes, 1290 Sauverny, Switzerland*
[5]*Departamento de Astronomía y Astrofísica, Pontificia Universidad Católica de Chile, Casilla 306, Santiago 22, Chile*
[6]*Las Cumbres Observatory Global Telescope, Goleta, CA 93117, USA*

Accepted 2011 November 9. Received 2011 November 9; in original form 2010 April 5

ABSTRACT

We present a new eclipsing post-common-envelope binary, identified inside the *Kepler* field prior to the launch of the spacecraft. Multifilter photometry and radial velocity data are analysed with an eclipsing-binary modelling code to determine the physical parameters of the binary. Spectra of the system within the primary eclipse and uneclipsed allow us to identify the spectral characteristics of the primary and secondary components. The primary component of the binary is a DA white dwarf, with $M \simeq 0.61\,\mathrm{M}_{\odot}$, $\log g \simeq 7.95$ and $T_{\rm eff} \simeq 20\,500$ K.

The detection of two flares and the emission signatures displayed in the spectra show that the secondary component of the system is chromospherically active and is classified as an active M4 main-sequence star. Its mass, radius and temperature are estimated as $M \simeq 0.39\,\mathrm{M}_{\odot}$, $R \simeq 0.37\,\mathrm{R}_{\odot}$ and $T_{\rm eff} \simeq 3200$ K. The ephemeris of the system is HJD = 245 3590.436 126(10) + 0.350 468 722(6) × E.

This binary is a new post-common-envelope binary (PCEB), with physical parameters within the range found in other systems of this small group of evolved binaries.

Key words: binaries: close – binaries: eclipsing – stars: late-type – white dwarfs.

1 INTRODUCTION

Short-period binaries composed of a white dwarf and a main-sequence star belong to the group known as post-common-envelope binaries (PCEB). The precursors of these systems are considered to be wide-separation binaries, where the more massive component evolves as a red giant and reaches the secondary, leading to a common envelope phase. Then, by friction, the orbital separation and orbital period decrease while the common envelope is ejected. Afterwards, the orbital evolution of the remnant system, composed of a white dwarf and a low-mass main-sequence star, enter into a stage dominated by slow angular momentum loss through magnetic breaking and gravitational radiation, eventually leading to a cataclysmic variable system when mass transfer from the cool secondary on to the white dwarf is initiated.

When the systems are properly aligned, the modelling of the photometric eclipses and radial velocity curves allows us to characterize the physical parameters of the components: radii, masses and effective temperatures. This is one of the very few cases in which the mass and radii of the white dwarfs can be measured independently if precise enough measurements are performed (e.g. Parsons et al. 2010). The values obtained can be used to test and validate our current knowledge of the stellar structure and evolution of both white dwarfs and low-mass main-sequence stars. Despite white dwarfs being the most abundant stellar remnants, only a handful or eclipsing systems are known. A list of the 14 known eclipsing binaries with components that are white dwarfs with cool main-sequence secondaries can be found in Pyrzas et al. (2009).

During a photometric wide-field survey at the 2.5-m Isaac Newton Telescope in 2005, we discovered a 18.8 R magnitude eclipsing object with a period of 8.4 h, eclipse duration of 28.5 min and ingress time of 1.1 min, revealing components with small radii. Follow-up spectroscopic observations allowed us to confirm that the components of the system are a white dwarf and an M main-sequence star. The object was identified in catalogues as USNO-B1.0 1377−0415424, 2MASS 19423720+4745486 and KIC–10544976, with coordinates (J2000) RA = $19^{\rm h}42^{\rm m}37\overset{\rm s}{.}20$, Dec. = $+47^{\circ}45'48\overset{''}{.}5$. The system was the only PCEB known to

⋆E-mail: josemanuel.almenara@oamp.fr

lie in the field of the *Kepler* space mission (Borucki et al. 2003) before the mission launch (two other systems containing eclipsing Jupiter-sized white dwarfs have been recently identified: Rowe et al. 2010; van Kerkwijk et al. 2010) and it is being observed continuously through a Guest Observer programme. We present in this work the discovery and follow-up photometric and spectroscopic observations that were performed in order to characterize the system. We analyse and model these observations to obtain the physical parameters of both components. The new system is composed of a white dwarf (also considered as the primary component throughout the paper) and a main-sequence M star (the secondary component).

2 OBSERVATIONS

2.1 Photometry

Photometric observations (summarized in Table 1) were performed using three telescopes at the Roque de los Muchachos Observatory: the 2.5-m Isaac Newton Telescope (INT), 4.2-m William Herschel Telescope (WHT) and 2.5-m Nordic Optical Telescope (NOT).

The INT data in the Sloan r' filter cover all the binary phases, including nine primary eclipses. With the WHT in service mode, we attempted to detect the secondary eclipse and a primary eclipse was observed at high cadence. The secondary eclipse is not detectable within the precision of our data. The NOT observation was made to measure the depth of the primary eclipse in various filters. A night at the IAC80 telescope was used to obtain calibrated magnitudes of the system.

All images were calibrated using standard IRAF procedures.

Close to the binary, two faint stars at 1.3 arcsec (NE) and 1.9 arcsec (NW) (see Fig. 1) were detected. To perform the photometry on the INT and WHT data affected by the two close contaminating stars, we used a non-circular aperture covering the three stars. Then, the flux contribution of each star was estimated by point spread function (*psf*) subtraction on a good seeing image. In the r' filter we found a relative contribution of 0.72 from the target and 0.15 and 0.13 from the 1.3-arcsec NE and 1.9-arcsec NW faint neighbours respectively. We made differential photometry with 7–11 reference stars, using custom IDL routines. The sky value was estimated from the mode around the apertures.

For the NOT data, collected in good seeing conditions, we performed *psf* photometry with the DAOPHOT (Stetson 1987) package in IRAF to obtain the magnitudes of the binary without contamination. Calibrated photometric magnitudes were obtained by differential photometry using stars of the field, calibrated with additional observations at the IAC80 telescope using Landolt stars. The results are given in Table 2, both at the minimum of the primary eclipse and uneclipsed.

2.2 Spectroscopy

In order to confirm the presence of a white dwarf in the system, one spectrum was obtained in 2007 with the ISIS spectrograph at the WHT telescope (31 per cent of the exposure was taken inside the eclipse). Later, the instrument DOLORES, at the 3.6-m Telescopio Nazionale Galileo Galilei (TNG), was used in 2008 to collect spectra at different orbital phases in order to obtain some radial velocity information. Also, two lower resolution spectra were observed in and out of eclipse for the determination of the spectral type of the secondary star. Due to the low precision of the radial velocity obtained with DOLORES, we again used the ISIS spectrograph in 2010 to obtain a precise radial velocity curve. The spectroscopic observations are summarized in Table 1. The reduction, wavelength calibration and extraction and flux calibration and normalization for the ISIS data were performed with standard IRAF tasks.

3 RESULTS

3.1 Ephemeris

We derived the ephemeris from the times of the minima of 10 eclipses: 6 from INT data in 2005, 3 from INT data in 2006 and one from WHT data in 2008. The WHT data have the shortest exposure time, so we obtain an eclipse model by fitting a trapezoid to these data. The trapezoid model was centred at different times near each of the eclipses with its corresponding eclipse depth (different for WHT and INT data). For each time, we interpolated the model to the observational points, taking the exposure time into account. The times of minima of each eclipse were calculated from the minima of χ^2. 1σ errors were derived from an increase of 1 over the minimum χ^2 value.

A linear fit to the epochs of 10 eclipses listed in Table 3 gives the ephemeris (with 1σ uncertainties in the last digit in parentheses) HJD $= 245\,3590.436\,126(10) + 0^{\rm d}.350\,468\,722(6) \times$ E, with an rms of the observed–calculated (O−C) of individual measurements against this ephemeris of 2.8 s.

3.2 Secondary eclipse

Assuming a circular orbit for the system, we searched for the secondary eclipse using the WHT Auxiliary Camera and the I filter. The observations were performed in service mode. A total of 43 images with an exposure time of 2 min were acquired. The filter I was chosen as a compromise between going too far into the red part of the spectrum, where the optical detectors are no longer sensitive, and having most of the flux coming from the M-dwarf component. Taking into account the depth of the eclipse of the white dwarf in the I band, measuring the contribution in this band of the contaminant stars and using the determined radii of the components given in Section 3.7, we estimate the depth of the secondary eclipse (the transit of the white dwarf in front of the M dwarf) to be of the order of 700 ppm. The differential photometry obtained using 10 stars close to the target shows some residual low-frequency noise and a dispersion of about 4000 ppm. We fitted a third-order polynomial to the region outside the expected secondary, and used this polynomial to normalize the light curve. A simple trapezoid model with the same duration and shape as the primary eclipses and different depths ranging from 0–5000 ppm was used to estimate the different significance levels by an evaluation of the change in χ^2. We do not detect the secondary eclipse. The 1σ upper limit to its depth is 1400 ppm, and the 3σ limit is 3400 ppm, thus consistent with the shallow expected depth.

3.3 Activity

Two flare events from the M secondary component can be identified in the 2005 INT observations. The first one was observed during the night of 2005 August 8 (see Fig. 2). The increment in flux was 13 per cent in the r' filter and the duration of the event was ∼35 min at orbital phase ∼0.25. The second flare event was observed at the end of the night of 2005 August 9 at orbital phase ∼0.32, with a duration of ∼15 min and a flux increment of 10 per cent.

Table 1. Summary of the photometric (top) and spectroscopy (bottom) observations.

Date (yyyymmdd)	Telescope	Instrument	Filter	Integration time (s)	Cycle time (s)	Pixel size ($''$)	Epoch	# data points
20050807							−0.104 to 0.329	
20050808							2.700 to 3.570	
20050809							5.517 to 6.299	
20050810							8.393 to 9.269	
20050811							11.295 to 12.079	
20050812	INT	WFC	r'	80	117	0.333	14.130 to 14.942	2030
20050814							19.820 to 20.643	
20060727							1009.952 to 1010.889	
20060728							1012.795 to 1013.735	
20060729							1015.696 to 1016.584	
20070403	IAC80	CAMELOT	U, B, V, R, I	2−1200	–	0.304	–	–
20080626	NOT	ALFOSC	U, B, V, R, I	10−360	–	0.38	3007.853 to 3008.115	4,5,10,8,8
20080812	WHT	ACAM	V	10	13	0.134	3141.925 to 3142.072	344
20080813			I	120	123		3144.419 to 3144.593	43

Date (yyyymmdd)	Telescope	Instrument	Wavelength range λλ	Integration time (s)	Dispersion (Å pix^{-1})	Resolution (Å)	Orbital phase
20070618	WHT	ISIS	4203−4950	1800	0.45	0.8	0.961
			7556−9199		0.99	1.7	0.960
			6316−7012	2×1800	0.32	1.3	0.467,0.535
20080805	TNG	DOLORES	4670−6687	7×1800	0.95	4.9	0.633,0.702,0.810,0.877,0.088,0.229,0.299
			5200−10200	2×1500	2.61	11.0	0.002,0.164
20100606	WHT	ISIS	3850−4600	13×1800,1×1088	0.22	0.7	0.183,0.250,0.318,0.386,0.453,0.525,0.600,
			7420−9000		0.49	1.5	0.667,0.735,0.803,0.877,0.945,0.013,0.069

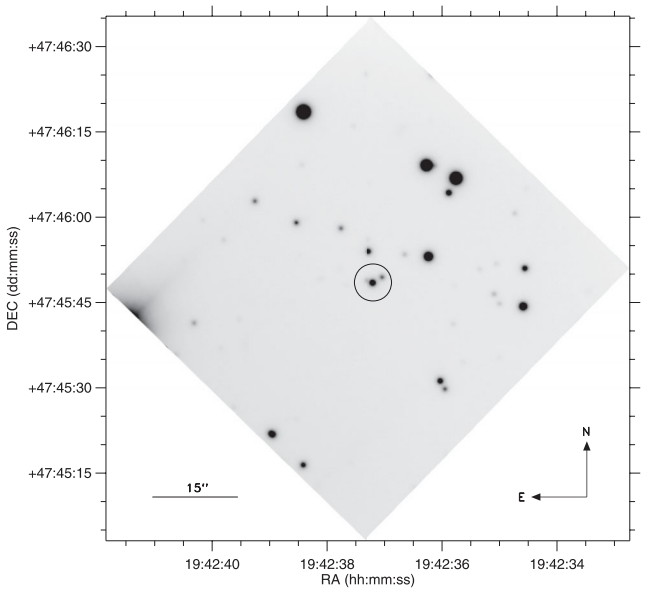

Figure 1. Finder chart image from WHT observations in the *I* filter. The circle marks the target and the two fainter close-neighbour stars.

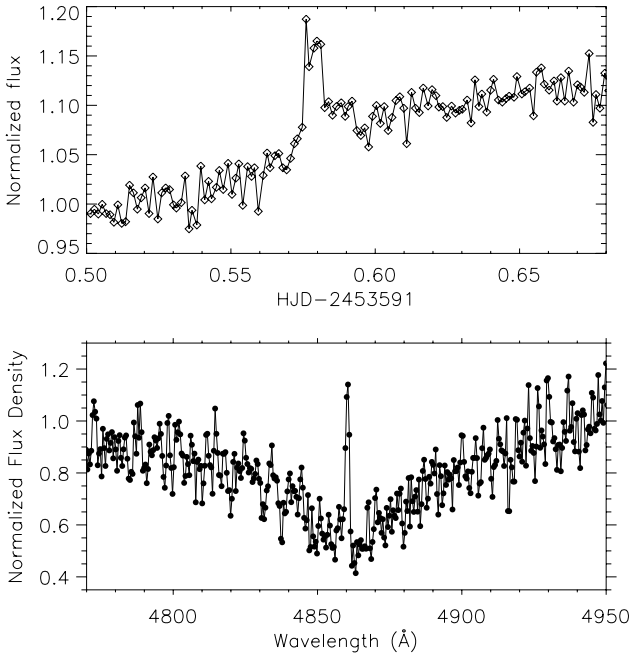

Figure 2. Signs of activity of the secondary star. Top: a flare observed with the r' filter at the INT on the night of 2005 August 8. Bottom: narrow Hβ chromospheric emission from the active secondary.

3.4 White dwarf spectrum

The collected WHT–ISIS blue spectra, in which most of the flux comes from the hot white dwarf, allowed us to compare the observed Balmer lines with pure hydrogen line-profile models (Koester 2010). We used combined 2010 WHT–ISIS blue spectra covering the Hζ, Hϵ, Hδ and Hγ Balmer lines and did not consider the Hβ line due to contamination from the secondary. To correct for the effect of Doppler shifts of each individual spectrum before building the combined one, we iterated the procedure assuming different white dwarf radial velocity semi-amplitudes. We interpolated the Koester models to 10^7 random $T_{\rm eff}$ and $\log g$ values and compared these with the data using χ^2. The combined spectrum was normalized for each trial model spectrum with a third-order polynomial. The Koester models were convolved with a Gaussian in order to match the resolution of the observed combined spectrum. We finally chose the combined spectrum that was built with a radial velocity semi-amplitude that minimized $\log g$. A bad radial velocity correction could result in a broadening of the lines in the combined spectrum, which has the same effect as increasing the surface gravity. For a radial velocity semi-amplitude of 130 km s^{-1} we obtained $T_{\rm eff} = 20400 \pm 200\,K$ and $\log g = 8.21 \pm 0.04$, with 1σ formal errors (see Fig. 3). Nebot Gómez-Morán et al. (2009) note that, having very similar formal errors to ours, a more realistic error in $\log g$ is around 0.2 dex.

Table 2. Calibrated apparent magnitudes of the system in and out of eclipse and the eclipse depth.

Filter	Out of primary eclipse (mag)	In primary eclipse (mag)	Δm (mag)
U	18.9 ± 0.2	–	–
B	19.5 ± 0.2	22.2 ± 0.3	2.72 ± 0.09
V	19.30 ± 0.05	20.9 ± 0.1	1.55 ± 0.05
R	18.83 ± 0.02	19.60 ± 0.05	0.77 ± 0.03
I	17.83 ± 0.03	18.05 ± 0.03	0.21 ± 0.02

3.5 The spectral type of the secondary component

In order to determine the spectral type of the secondary star, we used the spectra collected with the TNG-DOLORES spectrograph on-eclipse (when only the secondary component is visible) and the 2007 WHT–ISIS spectrum in the red range taken 69 per cent off-eclipse (see Fig. 4), where the contribution of the white dwarf is low. To derive the spectral type of the secondary component, we compare our spectra with a spectral library of low-mass dwarf templates (Bochanski et al. 2007), quantifying the differences and selecting the best solution by a χ^2 minimization procedure. From both the TNG-DOLORES and the 2007 WHT–ISIS spectra, the best fit is obtained with a template of an active M4V star.

Table 3. Minimum times of eclipses used in the ephemeris determination and difference against the linear ephemerides.

Epoch	HJD	O–C (s)
0	245 3590.436 13(2)	0.5 ± 2.0
3	245 3591.487 54(1)	1.0 ± 1.2
6	245 3592.538 95(5)	1.4 ± 4.2
9	245 3593.590 38(5)	2.7 ± 3.9
12	245 3594.641 81(7)	5.1 ± 5.7
20	245 3597.445 50(3)	0.4 ± 2.9
1010	245 3944.409 50(3)	-3.3 ± 2.7
1013	245 3945.460 94(7)	0.2 ± 5.6
1016	245 3946.512 29(2)	-5.0 ± 1.9
3142	245 4691.608 86(1)	0.9 ± 1.3

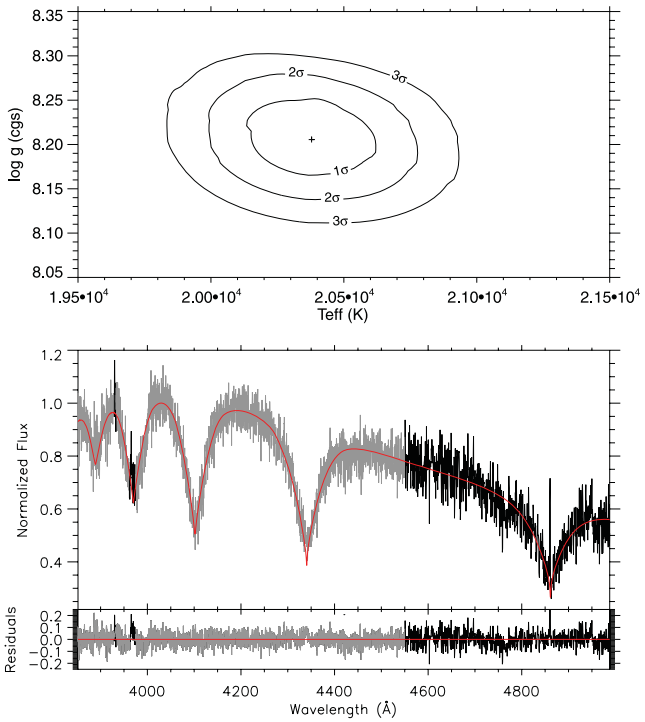

Figure 3. Top: 1, 2 and 3σ contours from the minimum χ^2 model in the $T_{\rm eff}$–$\log g$ plane. Bottom: the combined 2010 and 2007 WHT–ISIS blue spectrum (grey for the range used for the fit, black for the rest) with Hζ (3889 Å), Hϵ (3970 Å), Hδ (4102 Å), Hγ (4340 Å) and Hβ (4861 Å) Balmer lines, and an interpolated Koester pure hydrogen model for $T_{\rm eff} = 20\,400\,K$ and $\log g = 8.21$ (in red online). Both spectra were normalized at 4030 Å. Below, the residuals from the best-fitting Koester model.

3.6 Radial velocities

The radial velocity measurements of the secondary component (see Table 4) were obtained by shifting the M4V template (with the corresponding resolution) in velocity and comparing this with the observed spectrum with a χ^2 minimization procedure. We use diferent wavelength ranges for each set of data: 2007 WHT–ISIS red spectrum, TNG-DOLORES and 2010 WHT–ISIS red spectra.

The signal-to-noise ratio (SNR) of the TNG-DOLORES spectra is between 5 and 15, and we only succeeded in obtaining some measurements of the radial velocity of the secondary component using the region of Hα. It can be expected that the Hα emission should present an inhomogeneous distribution over the secondary star surface.

For the 2007 WHT–ISIS red spectrum we use a region between $\lambda\lambda$7650–8500 Å. This range includes the two duplets K I $\lambda\lambda$7664.90, 7698.96 Å and Na I $\lambda\lambda$8183.26, 8194.82 Å.

For the 2010 WHT–ISIS red spectra we use the Na I $\lambda\lambda$8183.26, 8194.82 Å lines. Due to the radial velocity precision and the complete phase coverage obtained in one night, only this last set of data was considered for the fitting.

The WHT–ISIS blue spectra do not have a suitable SNR to obtain the radial velocities of the primary.

3.7 Light and radial velocity curve fitting

The photometric and radial velocity data have been analysed using a code based on the Roche model; see Lázaro, Arévalo & Almenara (2009) for a description of it. The code allows us to fit multicolour photometric light curves and radial velocity curves simultaneously.

Depending on the seeing conditions, our photometry is affected by contamination by two faint stars close to the binary, more severely in some filters than in others. After some checks, we decided to fit the contaminated light curves, handling the contamination as a third light contribution that can be included in the model and optimized for each photometric band. We adopted as initial values the estimated contributions deduced from the *psf* photometric reduction, as explained previously.

To calculate the stellar surface fluxes of the primary component, a grid in ($T_{\rm eff}$, $\log g$, $M/{\rm M}_\odot$) from Holberg & Bergeron (2006), Kowalski & Saumon (2006), Bergeron et al. (2011) and Kremblay, Bergeron & Gianninas (2011)[1] for pure hydrogen white dwarfs has been adopted. This grid covers a range in surface gravity from 7.0–9.5 and a wide range in $T_{\rm eff}$, giving magnitudes in most of the common photometric bands including the *U, B, V, I* and Sloan r' used to collect our light curves. We use the $T_{\rm eff}$ and $\log g$ estimated in Section 3.4 as initial values for the primary star. While these initial values were determined from different white dwarf models as the ones used in the fit process, we will use the results of the fit with different models as a sanity check, as the fitted white dwarf parameters should be independent of the model used.

For the surface fluxes of the normal secondary star, a grid for solar metallicity from Lejeune, Cuisinier & Buser (1998) was adopted.

The photometric data were weighted according to the quality and phase coverage of the light curves. The r'- and V-band data were given the highest weights, as only these bands give well-sampled primary eclipses. The *B* and *I* data, with just a few points

Table 4. Radial velocity of the secondary star, deduced from the TNG-DOLORES and WHT–ISIS spectra.

HJD	Phase	RV (km s^{-1})	Instrument	Line
2454270.682060	0.9605	-81 ± 6	ISIS	K I–Na I
2454684.412676	0.4670	42 ± 9	DOLORES	Hα
2454684.436438	0.5348	-41 ± 19	DOLORES	Hα
2454684.470906	0.6331	-210 ± 16	DOLORES	Hα
2454684.495084	0.7021	-206 ± 21	DOLORES	Hα
2454684.532920	0.8101	-199 ± 28	DOLORES	Hα
2454684.556380	0.8770	-103 ± 29	DOLORES	Hα
2454684.630189	0.0876	107 ± 28	DOLORES	Hα
2454684.679679	0.2288	193 ± 17	DOLORES	Hα
2454684.704436	0.2995	266 ± 29	DOLORES	Hα
2455354.409228	0.1827	160 ± 13	ISIS	Na I
2455354.432979	0.2505	160 ± 10	ISIS	Na I
2455354.456693	0.3181	151 ± 9	ISIS	Na I
2455354.480380	0.3857	115 ± 8	ISIS	Na I
2455354.504098	0.4534	47 ± 8	ISIS	Na I
2455354.529266	0.5252	-40 ± 8	ISIS	Na I
2455354.555415	0.5998	-123 ± 6	ISIS	Na I
2455354.579140	0.6675	-172 ± 7	ISIS	Na I
2455354.602846	0.7351	-181 ± 5	ISIS	Na I
2455354.626571	0.8028	-172 ± 6	ISIS	Na I
2455354.652676	0.8773	-126 ± 6	ISIS	Na I
2455354.676372	0.9449	-70 ± 6	ISIS	Na I
2455354.700052	0.0125	-6 ± 8	ISIS	Na I
2455354.719947	0.0693	68 ± 12	ISIS	Na I

[1] See http://www.astro.umontreal.ca/~bergeron/Codingmodels

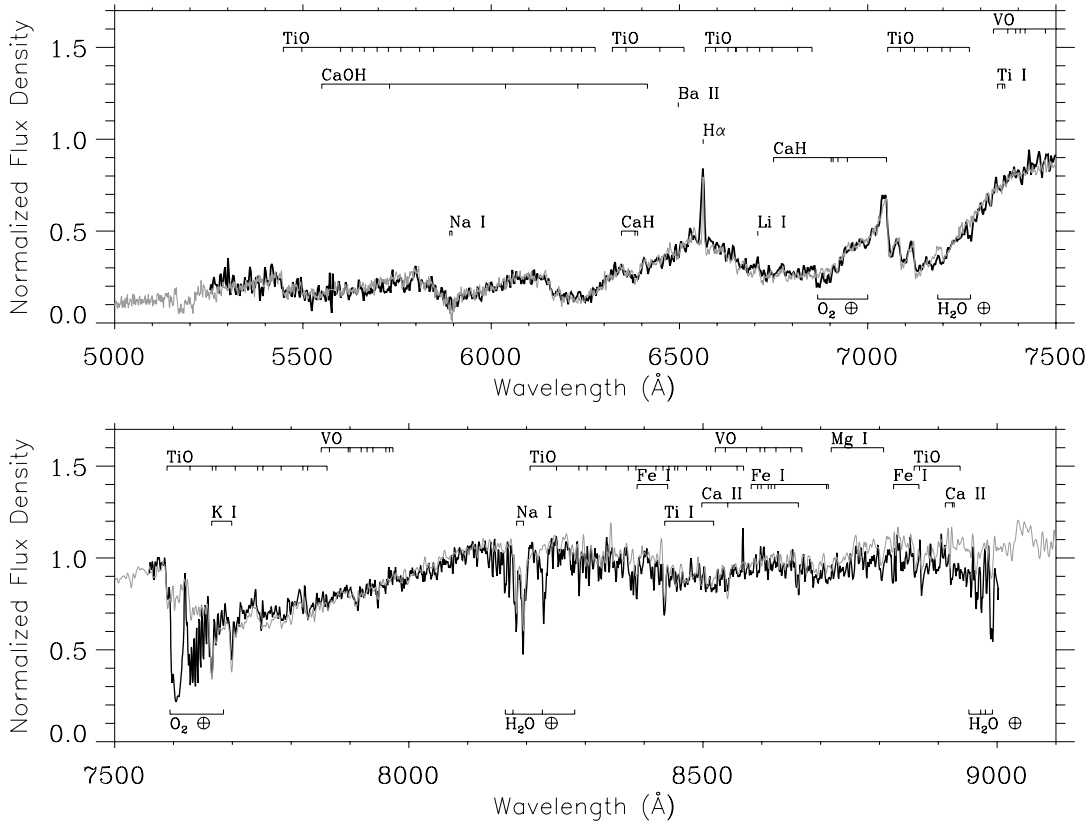

Figure 4. DOLORES on-eclipse spectrum (top), the ISIS red spectrum (bottom) and the active M4V template (in grey). Some relevant spectral features are labelled (Fay, Stein & Warren 1974; Kirkpatrick, Henry & McCarthy 1991).

within and out of eclipse, even if contributing to determine the colours of the stars, were given a low weight in the fits. The adopted relative weights were 0.05, 0.5, 1.0 and 0.05 for B, V, r' and I data respectively.

As the primary star is nearly a point source as seen from the secondary and the irradiation of the secondary over the primary is negligible, we have used the simple mode of irradiation in the code modelling. The bolometric albedo $A_{\rm b,2}$ and gravity-darkening coefficient β_2 of the secondary star were fixed to the standard values for convective atmospheres: $A_{\rm b,2} = 0.50$, $\beta_2 = 0.08$.

The system presents a rather moderate heating effect in the internal hemisphere of the secondary component due to the irradiation of the hot white dwarf, with a maximum difference of less than 200 K between the surface temperatures. Therefore we have not applied any correction to the measured radial velocities derived from the absorption lines. The code corrects for the exposure time of the spectrum used to obtain each radial velocity measurement. We have assumed orbital eccentricity $e = 0$ and synchronous rotation of the stars.

The free parameters in the model were the masses (M_1, M_2), the filling factors (determining the radii R_1, R_2) and effective temperatures ($T_{\rm eff,1}, T_{\rm eff,2}$) of the two stellar components, plus the orbital inclination angle (i), the third light contribution in each photometric band (F_{3,λ_j}) and the radial velocity of the centre of mass of the binary ($Vr_{\rm cm}$). The modelling of the observed light and radial velocity curves is posed as a non-linear least-squares fit, with a measure of goodness-of-fit χ^2 defined as

$$\chi^2 = \sum \frac{1}{\sigma_i^2} \left(Y_{\rm o_i} - Y_{\rm m_i}\right)^2 + \sum \frac{1}{\sigma_j^2} \left(V_{\rm o_j} - V_{\rm m_j}\right)^2,$$

where $Y_{\rm o_i}$ and $Y_{\rm m_i}$ are the observed and model light curve at each orbital phase and $1/\sigma_i^2$ the weight associated with the data point, while $V_{\rm o_j}$ and $V_{\rm m_j}$ are the observed and model radial velocity points and $1/\sigma_j^2$ the corresponding weight.

As the low SNR of our blue spectra did not allow us to obtain a radial velocity curve of the primary star, the mass of the white dwarf component is only indirectly fixed by the modelling of the light curves and the radial velocity of the secondary component.

In Table 5 we present the parameters derived from the optimal solution to our photometric radial velocity data, while in Figs 5 and 6 the fits are displayed. The errors shown in the table are the formal random errors of the fit only. Systematic errors will also be present due to the models applied, but these cannot be computed. The estimated contribution of the third light (out of eclipse) resulting from the fit amounts to 4 per cent in B, 19 per cent in V, 18 per cent in r' and 20 per cent in the I band. The fitted values of the $T_{\rm eff}$ and $\log g$ of the white dwarf in the combined analysis are quite similar to the initial values that were estimated from the spectral analysis of Section 3.4, which is a good sign of consistency. There is a slight difference in $\log g$, as the combined fit converges to smaller values. A $\log g$ of 8.21 would require slightly lower temperatures for the secondary, which would be more compatible with a M6V spectral type. This shows that the formal errors of Section 3.4 are indeed not realistic and a more reasonable estimation of the accuracy of the $\log g$ measurement is 0.3 dex, which was adopted in Table 5.

The luminosity and absolute bolometric magnitudes are derived from the effective temperatures and radii, adopting $\rm M_{bol,\odot} = +4.74$. The bolometric absolute magnitude of the primary star, $M_{\rm bol,1} = 8.61$, is about 0.15 mag brighter than the value listed in

Table 5. Results of the simultaneous fit of *BVrI* light and RV curves, with 1σ formal errors.

	Primary	Secondary
Effective temperature	$T_{\rm eff1} = 20470 \pm 1300$ K	$T_{\rm eff2} = 3200 \pm 100$ K
Surface gravity	$\log g_1 = 7.95 \pm 0.04$	$\log g_2 = 4.93 \pm 0.06$
Equivalent radius	$R_{\rm eq.,1}(\rm R_\odot) = 0.0136 \pm 0.0005$	$R_{\rm eq.,2}(\rm R_\odot) = 0.37 \pm 0.02$
Mass	$(M/\rm M_\odot)_1 = 0.61 \pm 0.04$	$(M/\rm M_\odot)_2 = 0.39 \pm 0.03$
Luminosity	$(L/\rm L_\odot)_1 = 0.029 \pm 0.003$	$(L/\rm L_\odot)_2 = 0.013 \pm 0.002$
Absolute magnitude	$M_{V,1} = 10.6 \pm 0.34$	$M_{V,2} = 11.9 \pm 0.33$
Radial velocity semi-amplitude		$K_2 = 183 \pm 5\,\rm km\,s^{-1}$
Systemic radial velocity	$Vr_{\rm cm} = -8.5 \pm 3\,\rm km\,s^{-1}$	
Orbital inclination	$i = 89.^\circ6 \pm 1.5$	
Semi-major orbital axis	$a = 2.10 \pm 0.04\,\rm R_\odot$	

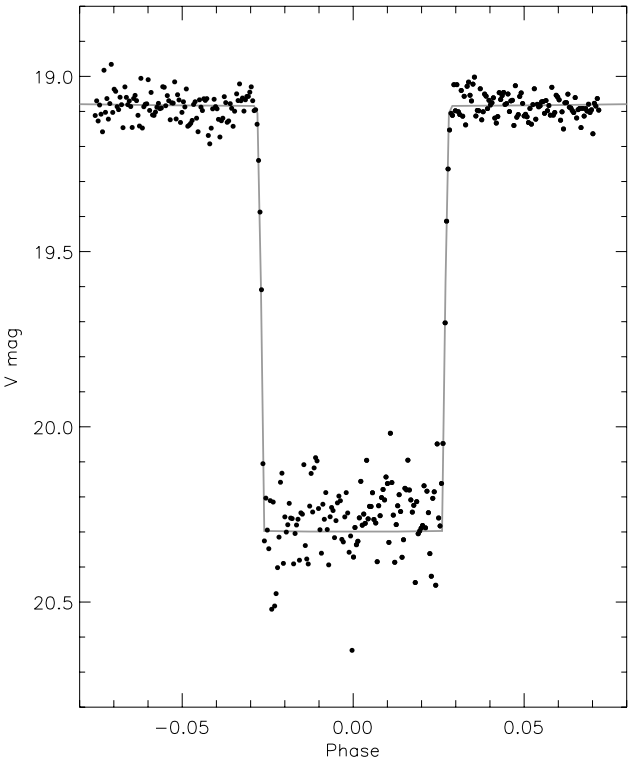

Figure 5. Observed eclipse in the *V* filter with the WHT and the model fit.

Holberg & Bergeron (2006), Kowalski & Saumon (2006), Bergeron et al. (2011) and Tremblay et al. (2011) for a white dwarf of mass $M = 0.62\,\rm M_\odot$, $T_{\rm eff} = 20\,000$ K and $\log g = 8.0$, but in reasonable agreement given the uncertainties and the fact that our derived temperature is about 500 K hotter. On the other hand, adopting the bolometric correction $BC = -2.00$ from the table of Holberg & Bergeron (2006), Kowalski & Saumon (2006), Bergeron et al. (2011) and Tremblay et al. (2011), our $M_{\rm bol,1}$ implies $M_{V,1} = 10.61$. Its mass and radius locate it very close to the zero-temperature mass–radius relation presented in Verbunt & Rappaport (1988).

For the secondary cool component, the derived mass and radius are close to the solar-metallicity theoretical isochrones of Baraffe et al. (1998) and similar to other empirical determinations of the mass and radius of low-mass stars, as displayed in fig. 17 of Parsons et al. (2010). The value of the absolute magnitude of the secondary star seems compatible with the expected magnitudes for normal M dwarfs with a spectral type around M4V. However, the absolute visual magnitude of the cool dwarfs increases rapidly with decreasing effective temperature, changing from $M_V = +11.3$ to $+13.5$ between $T_{\rm eff} \simeq 3370$ and 3050 K (Schmidt-Kaler 1982). Rather discrepant values of M_V can be found in the literature for M dwarfs of the same spectral type or temperature. From fig. 12 of Casagrande, Flynn & Bessell (2008), for M dwarfs with metallicity within $-0.1 <$ [M/H] < 0.1, at an effective temperature $T_{\rm eff} \simeq 3200\,KM_{bol}$ values in the range 8.50–9.0 can be estimated, which translates to an absolute visual magnitude $M_V \simeq 11.0$–11.5. Then, given the uncertainties, the $M_{V,2}$ given in Table 5 seems normal.

Regarding the distance of the new system, the errors in our photometry plus the third-light contamination in the light curves make any estimation of $E(B-V)$ based on the comparison between the reddened model and the observed colours unreliable. Therefore, we rely on the comparison between the derived absolute visual magnitude of the secondary star $M_{V,2}$ and the calibrated V magnitude within the primary eclipse free of contaminating third light, given in Table 2, which must correspond to the apparent magnitude of the cool component. Adopting a bolometric correction $BC = -2.5$ from (Lejeune et al. 1998) and an error in $BC \simeq 0.3$ due to the uncertainty in $T_{\rm eff,2}$, the estimated absolute visual magnitude of the secondary star is $M_{V,2} = 11.9 \pm 0.3$. The range of colour excess $E(B-V) = 0.0$–0.10 produces colours compatible with the data, $E(B-V) \simeq 0.05$ being slightly better. The Schlegel, Finkbeiner & Davis (1998) maps of extinction limit the reddening in the direction of our system to $E(B-V) \leq 0.10$. Adopting $E(B-V) = 0.05$, the apparent V magnitude during the eclipse and the derived $M_{V,2}$ of the secondary star, we estimate the distance to the system as $d \simeq 590 \pm 100$ pc.

To estimate the formal statistical errors of the fitted parameters, we performed 4000 different fits to the light and radial velocity curves, starting with random initial values. A Gaussian was fitted to the histogram of the final parameters in the different realizations and we put the 1σ value as the error in Table 5. These formal errors provide generally small values, because among other things it is difficult to include the errors in the models. As an example, the difference between $\log g_1$ obtained in Section 3.4 and that obtained in this section is 0.3, which gives an idea of a more realistic value for the errors.

4 CONCLUSIONS

The newly discovered variable USNO-B1.0 1377−0415424, 2MASS 19423720+4745486 and KIC–10544976 is a post-common-envelope eclipsing binary system, which seems to be

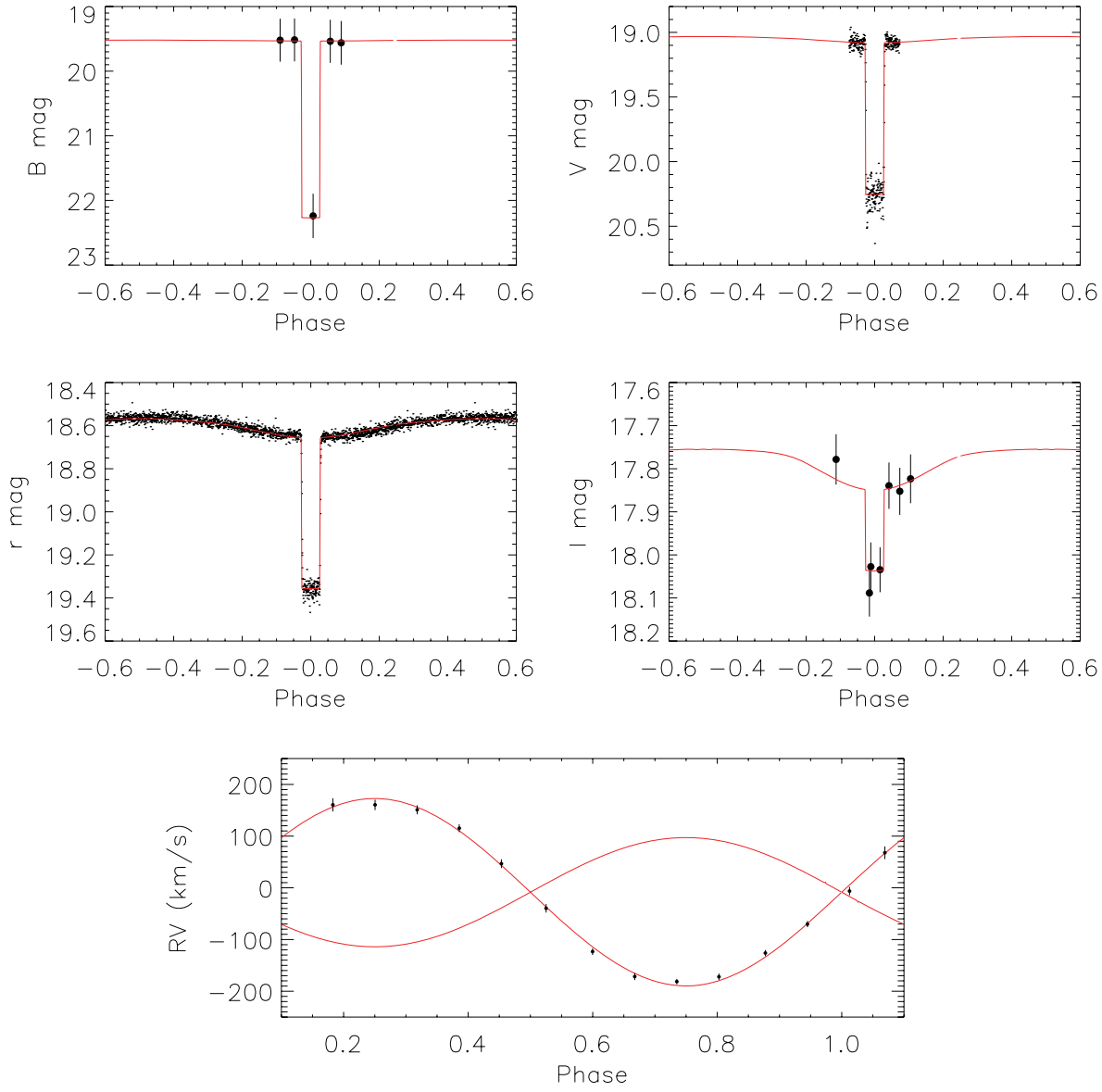

Figure 6. Upper: *B* (NOT), *V* (WHT), r' (INT) and *I* (NOT) observed light curves with error bars and simultaneous model fits. Lower: radial velocity of the secondary component with estimated error bars, from 2010 WHT–ISIS data. The modelled *centre-of-mass* orbital velocity is shown for the two stars.

composed of a primary DA white dwarf and an active M4V secondary star. The activity of the cool component is revealed photometrically as flares and spectroscopically as chromospheric emission in the Balmer lines.

We have presented photometric data in the *UBVr′I* bands, with a well-sampled and complete phase-coverage light curve in the r' Sloan filter and partial coverage in the other bands. A radial velocity curve of the secondary star has been obtained, based on the Na I lines of the M dwarf, as the Hα line seems to be contaminated by chromospheric emission.

The photometric and radial velocity curves have been analysed using an eclipsing-binary code to deduce the physical parameters of the stellar components. The masses and radii of the stellar components have been derived without using any theoretical mass–radius relation. We find that the primary star looks like a DA white dwarf, with mass $M = 0.61\,\mathrm{M}_{\odot}$, gravity $\log g = 7.95$ and temperature $T_{\rm eff} = 20\,500$ K. The spectrum of the chromospherically active secondary star resembles an active M4 main-sequence star. From the light and radial velocity curve fits, we determine its mass, radius, temperature and $\log g$: $M = 0.39\,\mathrm{M}_{\odot}$, $R = 0.37\,\mathrm{R}_{\odot}$, $\log g \simeq 4.93$ and $T_{\rm eff} = 3200$ K. The physical parameters of both stellar components are within the range of values found in other PCEB systems. The main sources of uncertainty in the derived parameters are the quality of our photometric data and the lack of radial velocity data for the primary star, which would allow us to fix the masses for both stellar components independently of the photometric data.

This object is the only one of its type known so far inside the field of view of the *Kepler* mission (Borucki et al. 2008) launched in 2009 March. *Kepler* will observe this object with a 1 min cadence over one year. It is planned to survey more than 1000 eclipses yr^{-1} with *Kepler*, which will allow us to study the interaction among the components in unprecedented detail (reflected light, ellipsoidal deformations) as well as the activity of the secondary star (flares, stellar spots). *Kepler* data will also allow a significantly improved timing of the eclipses, which may be indicative of any period change resulting from variations in the moments of inertia, mass transfer

or the influence of orbiting third masses. We may therefore expect that this object will become a reference object for eclipsing post-common-envelope binaries, despite its relative faintness.

ACKNOWLEDGMENTS

This article is based on observations made with the INT, NOT, WHT and TNG operated on the island of La Palma by the IAC in the Spanish Observatorio del Roque de los Muchachos and with the IAC80 operated on the island of Tenerife by the IAC in the Spanish Observatorio del Teide.

Based on service observations made with the WHT operated on the island of La Palma by the Isaac Newton Group in the Spanish Observatorio del Roque de los Muchachos of the Instituto de Astrofísica de Canarias.

We thank P. Rodríguez-Gil and A. Rebassa-Mansergas for observing the object with ISIS at the WHT.

This paper makes use of data obtained from the Isaac Newton Group Archive, which is maintained as part of the CASU Astronomical Data Centre at the Institute of Astronomy, Cambridge.

Some data presented here have been taken using ALFOSC, which is owned by the Instituto de Astrofísica de Andalucía (IAA) and operated at the Nordic Optical Telescope under agreement between IAA and the NBIfAFG of the Astronomical Observatory of Copenhagen.

We thank D. Koester, who kindly provided the white dwarf atmosphere models.

Balmer/Lyman lines in the models were calculated with the modified Stark-broadening profiles of Tremblay & Bergeron (2009), kindly made available by the authors.

JMA and HJD acknowledge support by grants ESP2004-03855-C03-03 and ESP2007-65480-C02-02 of the Spanish Ministerio de Ciencia e Innovación.

REFERENCES

Baraffe I., Chabrier G., Allard F., Hauschildt P. H., 1998, A&A, 337, 403
Bergeron P. et al., 2011, ApJ, 737, 28
Bochanski J. J., West A. A., Hawley S. L., Covey K. R., 2007, AJ, 133, 531
Borucki W. J. et al., 2003, Proc. SPIE, 4854, 129
Borucki W. et al., 2008, in Sun Y.-S., Ferraz-Mello S., Zhou J.-L., eds, IAU Symp. 249, Exoplanets: Detection, Formation and Dynamics. Cambridge Univ. Press, Cambridge, p. 17
Casagrande L., Flynn C., Bessell M., 2008, MNRAS, 389, 585
Fay T. D., Jr, Stein W. L., Warren W. H., Jr, 1974, PASP, 86, 772
Holberg J. B., Bergeron P., 2006, AJ, 132, 1221
Kirkpatrick J. D., Henry T. J., McCarthy D. W., Jr, 1991, ApJS, 77, 417
Koester D., 2010, Mem. Soc. Astron. It., 81, 921
Kowalski P. M., Saumon D., 2006, ApJ, 651, L137
Lázaro C., Arévalo M. J., Almenara J. M., 2009, New Astron., 14, 528
Lejeune T., Cuisinier F., Buser R., 1998, A&AS, 130, 65
Nebot Gómez-Morán A. et al., 2009, A&A, 495, 561
Parsons S. G., Marsh T. R., Copperwheat C. M., Dhillon V. S., Littlefair S. P., Gänsicke B. T., Hickman R., 2010, MNRAS, 402, 2591
Pyrzas S. et al., 2009, MNRAS, 394, 978
Rowe J. F. et al., 2010, ApJ, 713, L150
Schlegel D. J., Finkbeiner D. P., Davis M., 1998, ApJ, 500, 525
Schmidt-Kaler Th., 1982, in Schaifers K., Voigt H. H., eds, Landolt-Börnstein, Neue Serie, Vol. 6.2b. Springer–Verlag, Berlin
Stetson P. B., 1987, PASP, 99, 191
Tremblay P.-E., Bergeron P., 2009, ApJ, 696, 1755
Tremblay P. E., Bergeron P., Gianninas A., 2011, ApJ, 730, 128
van Kerkwijk M. H., Rappaport S. A., Breton R. P., Justham S., Podsiadlowski P., Han Z., 2010, ApJ, 715, 51
Verbunt F., Rappaport S., 1988, ApJ, 332, 193

This paper has been typeset from a TEX/LATEX file prepared by the author.